Interdiffusion of Elements During Ultrasonic Additive Manufacturing

MICHAEL PAGAN, CHRISTIAN PETRIE, DONOVAN LEONARD,
NIYANTH SRIDHARAN, STEVEN ZINKLE, and SUDARSANAM SURESH BABU

This paper reports evidence for enhanced elemental interdiffusion during ultrasonic additive manufacturing (UAM) across metal boundaries of copper-aluminum, nickel-gold, and nickel-gold-aluminum. The high solute interdiffusion measured by energy dispersive X-ray spectroscopy line scans is rationalized with calculated vacancy concentrations orders of magnitude larger than thermal equilibrium values. The above estimates are supported by existing knowledge related to defect physics and UAM thermal cycles. The observation of pronounced elemental mixing are evidence for the presence of enhanced non-equilibrium immiscible metal interdiffusion during UAM processing.

https://doi.org/10.1007/s11661-020-06131-2
© The Minerals, Metals & Materials Society and ASM International 2021

I. INTRODUCTION

THIS research was motivated by the unexpected experimental observation of pronounced interdiffusion during the routine characterization of metallized fiber optics to create smart structures for nuclear reactor applications.[1] These smart structures were produced by embedding optical fibers using ultrasonic additive manufacturing (UAM).

The UAM process, initially developed by White,[2,3] is the method by which a 3D metal component is fabricated through cyclic additive and subtractive operations. This is schematically illustrated in Figure 1. During additive operations, foil tape layers (~ 150 μm thick) are bonded to each other and to a substrate through a solid-state process that relies on high strain rate (up to 10^5 s^{-1}[4]) ultrasonic oscillations (20 kHz) without melting. The ultrasonic vibrations are applied using a rolling cylindrical horn called a *sonotrode*. The sonotrode simultaneously applies a downward force on the foil (in the *z*-direction) and laterally scrubs (in the *y*-direction) as it traverses forward (in the *x*-direction). This is shown below in Figure 1(a). The ultrasonic vibrations from the sonotrode cause the localized surface asperities to deform plastically and the surface oxides at the interface of the foils to break down. This operation creates two atomically clean surfaces that bond at temperatures significantly below their respective melting temperatures.[5] This is shown below in Figure 1(b). The additive layering operations are alternated with subtractive operations using a computer numerical controlled (CNC) mill to remove unwanted material. In this way, a near net shape 3D component can be fabricated.[6–10] Many advantages to this manufacturing approach stem from the relatively short fabrication times and low processing temperatures. Some applications that have taken advantage of UAM include bonding dissimilar or difficult-to-weld metals[9,11] and embedding fragile materials, such as ceramics or sensors.[12] Optical fiber strain sensors can be embedded through exploiting the alternating additive and subtracting operations in the following manner. The additive process is paused after several foil layers have been added to the substrate, then the CNC mill is used to cut an optical fiber sized channel (straight or curved) into the top foil. The optical fiber can then be placed into this channel and the additive process is resumed adding more foil layers on top of the now embedded optical fiber.[1,13,14] This is shown below in Figure 1(c).

UAM is similar to other solid-state welding techniques in the sense that it relies on plastic deformation to achieve oxide dispersion and bring about nascent metal contact which are necessary conditions for solid-state welding to occur.[10,11,15] However, it remains unclear whether this joining process occurs with significant macroscopic heat generation, as is the case with friction welding and friction stir welding. This is primarily due to the difficulties in conducting measurements at the time scales involved in UAM.[16,17]

MICHAEL PAGAN is with the University of Tennessee, Knoxville, TN 37996. Contact e-mail: mpagan1@vols.utk.edu CHRISTIAN PETRIE, DONOVAN LEONARD, and NIYANTH SRIDHARAN, are with the Oak Ridge National Laboratory, Oak Ridge, TN 37831. STEVEN ZINKLE and SUDARSANAM SURESH BABU are with the University of Tennessee and also with the Oak Ridge National Laboratory.

Manuscript submitted April 17, 2020; accepted December 13, 2020.
Article published online February 8, 2021

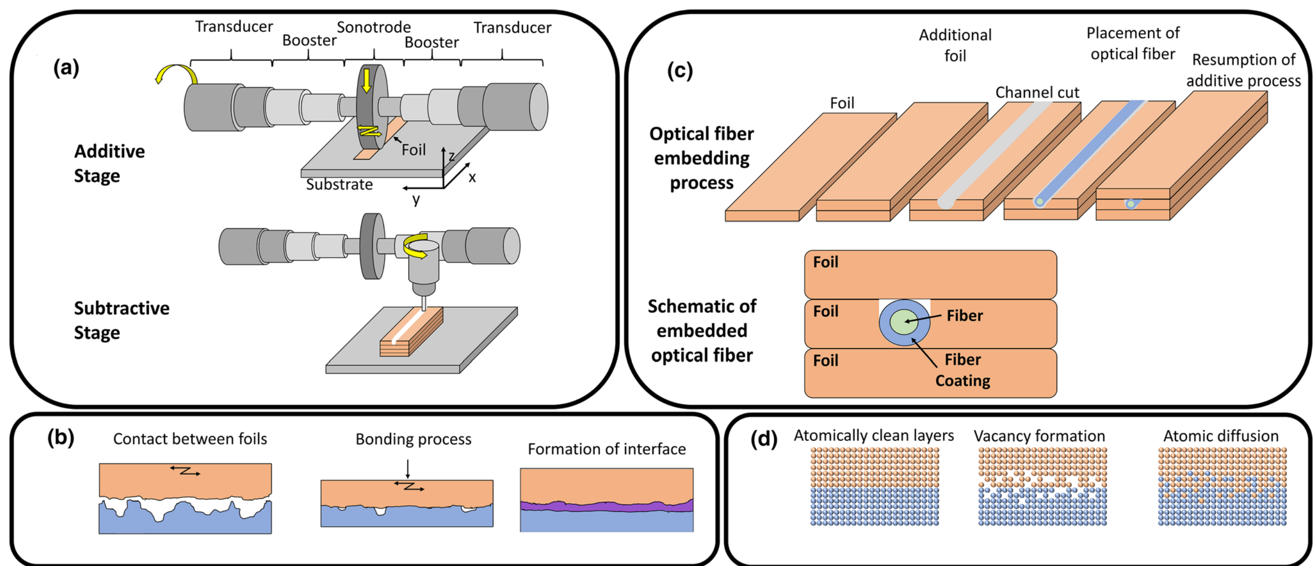

Fig. 1—Schematic of UAM process. (*a*) Overview of the additive and subtractive stages, (*b*) optical fiber embedding process, (*c*) micrometer level bonding process, and (*d*) atomic level bonding process.

However, recent theoretical calculations have shown that the interface temperatures may exceed the recrystallization temperature (*i.e.*, 50 pct melting point temperature in Kelvin). These observations have been confirmed with detailed microscopy of the weld interfaces which show grain refinement corresponding to a dynamic recrystallization.[18–22] However, literature also postulates that during joining of dissimilar metals, high strain rate deformation through UAM may affect elemental interdiffusion through elevated concentrations of vacancies.[23] This hypothesis is also illustrated schematically in Figure 1(d).

Additionally, the microscopic interface interactions between the UAM foils and fiber optic metal coatings have received limited attention in lieu of the technical demonstrability of the fiber optic embedding process. The full technical implementation of embedded fiber optics for nuclear applications mandates a scientific understanding of the material interactions during the embedding process.

Embedding fiber optic sensors with UAM is intriguing because the sensors can be used for spatially distributed strain monitoring for various applications.[13,24–29] Although fiber optic mechanisms are not this paper's focus, several fundamentals are briefly reviewed for context. The conventional polymer coatings of fiber optics could survive the UAM embedding process,[30] although they are unsuitable for performance in harsh environments, such as high temperature, high-radiation fluence, and chemically reactive environments limiting the end use. Thus, optical fibers embedded into structural materials in these demanding environments must have the polymer coating stripped away and replaced with a metal coating.[13,14] The process of coating an optical fiber (*metallization*) can be performed through electroplating (for copper or gold coatings) or through electroless deposition (for nickel coatings).[26,31,32] Since the UAM process allows dissimilar metals to bond, the optical fiber can be coated with any metal required for its specific application. The exact mechanisms of dissimilar metal welding under these geometrical constraints are not clear. Previous UAM work has shown that similar metals[8,33] and dissimilar metals undergo intense plastic deformation at the interface to induce bond formation.[15,34,35] Almost all literature show that the plastic deformation is localized almost entirely in the softer metal.[15,34–36] However, whether the extensive plastic deformation could contribute to enhanced interdiffusion is still not clear. Previous multi-scale characterization of high strain rate solid-state impact welds made with steel and aluminum showed extensive interdiffusion of elements due to localized diffusion promoted by melting.[37] However, similar studies performed on UAM samples did not show any significant interdiffusion.[38] One can rationalize these differences based on differences in the extent of adiabatic heating between these two processes.

In the case of high strains induced during accumulative roll bonding (ARB) where two metal sheets are joined in the solid state by cold rolling, significant interdiffusion has been documented. The unique results observed in ARB refinement include remarkable deviation from thermodynamic equilibrium. In composite structures, such as Cu-Nb layers, mechanical alloying of the immiscible phases was found. The previously sharp interface boundary between the copper and niobium widened as both elements appear intermixed. Although research is still underway in this field, the models used to explain this phenomenon include ballistic mixing and other non-equilibrium diffusion processes, such as plasticity-driven mechanical mixing and severe plastic deformation, SPD.[39,40] While the overall strains may be comparable to the UAM process, the ARB strain rate at which the deformation occurs is over 3 orders of magnitude lower.

Gunduz *et al*.[23] investigated the possibility of interdiffusion in ultrasonic welding using an aluminum and zinc dissimilar metal pair. The authors performed energy dispersive X-ray spectroscopy (EDS) analyses in a scanning electron microscope (SEM) and showed the presence of a micron scale interdiffusion zone. Interestingly, Gunduz *et al.* assumed there was no temperature increase during bonding and concluded that the diffusion profile must be linked to a strain rate induced vacancy concentration of up to 0.07 atomic fraction. This assumption would lower the local melting temperature and increase the interdiffusivity by a factor of 10^5. Currently, researchers in the field disagree on the mechanism of interdiffusion seen across UAM interfaces. Chen *et al*.[19] accepted the Gunduz *et al.* claim that an increased vacancy concentration and associated diffusivity could exist for their alloy system even though their experiment had higher welding temperature. With an increase in temperature the vacancy annihilation rate could also be enhanced. Fujii *et al*.[22] used the Gunduz *et al.* claim of an elevated vacancy concentration to rationalize how recrystallization could occur at lower temperatures. However, Fujii *et al.* could not calculate a vacancy concentration as high as Gunduz *et al.* Ward and Cordero[41] criticized the Gunduz *et al.* assumption of the absence of a temperature rise and the extremely high vacancy concentration (~ 10^{-1}) citing that it would destabilize the crystalline lattice. Instead, Ward and Cordero[41] modeled the UAM interface using elevated temperatures and thermodynamically equilibrium vacancy concentrations. Sietins *et al*.[42] used high-resolution transmission electron microscopy (TEM) EDS techniques to observe UAM interfaces. Based on these measurements, the authors attributed the interdiffusion to bulk diffusion without invoking elevated vacancy concentration arguments. Other low-resolution SEM observations of UAM interfaces[15,43–45] have also conceded that due to the spatial resolution of the equipment being used, significant diffusion could not be resolved. Based on this literature review, one can conclude that there are disagreements in the community with regard to interdiffusion occurring across UAM interfaces.

Therefore, the scope of this research study pertains to interdiffusion of elements from the coatings of the fiber optic strain gauges into the foils during UAM and rationalization of the same using physics of interdiffusion.

II. EXPERIMENTAL PROCEDURE

A. *Introduction to Fibers and Coatings*

Three sets of samples were evaluated: the Al-Cu sample, the Ni-Au sample, and the Al-Au-Ni sample. The Al-Cu sample configuration was based on an optical fiber electroplated with copper (20 μm ± 5 μm) (CU1300 fiber from IVG Fiber), embedded into Al-6061 foils using UAM. Two interfaces from the Al-Cu samples were analyzed. In addition, an optical fiber with electroplated copper before the embedding process, called the *copper baseline sample*, was also considered as a baseline. The cross-sectional areas of the electroplated copper regions were characterized before and after the embedding process. The Ni-Au sample configuration was based on an optical fiber electroplated with gold (15 ± 5 μm) (ASI9.0/125/155G fiber from Fiberguide Industries), which was then embedded into Ni-200 foils using UAM. An optical fiber with electroplated gold, called the *gold baseline sample*, was also considered as a baseline for comparison before the embedding process. The Al-Au-Ni sample configuration had an optical fiber coated with nickel (1.5 to 5 μm) through an electroless process, then immersed in gold (ENIG) (0.15 to 0.20 μm) (3896 fiber from OZ Optics), and then embedded into Al-6061 foils using UAM. Two bi-layer interface combinations (*i.e.*, Al-Cu and Ni-Au) and one tri-layer interface combination (*i.e.*, Al-Au-Ni) were explored. All the SEM images from the interface regions were analyzed using Image-J software.

B. *UAM Processing Conditions*

All samples were produced using a 9 kW UAM machine at Fabrisonic LLC (Columbus, OH) using 150 μm thick × 25.4 mm wide foils. During UAM processing of the Al-Cu and the Al-Au-Ni samples, the sonotrode horn exerted a downward force (in the z-direction) of 4000 N and traveled forward (in the x-direction) at a speed of 0.033 m/s with a horizontal oscillation amplitude (in the y-direction) of 28 μm. For the Ni-Au sample, the sonotrode horn exerted a downward force of 7000 N and traveled forward at a speed of 0.022 m/s with a horizontal oscillation amplitude of 38 μm. During all the above experiments, the sonotrode vibrations were set at a frequency of 20 kHz. The estimated temperature profile was extracted from the non-dimensional data published by Sriraman *et al*.[16] using WebPlotDigitizer software.[46] Fifty data points were extracted and extrapolated by setting the maximum temperature as described in Section III–D and setting the room temperature at 298 K. After the fabrication process, samples were cut in different sections, cold mounted in epoxy, and polished to a 0.05 μm finish using standard metallography techniques.

C. *Optical and Electron Microscopy*

For the optical microscopy, a Zeiss AxioCam 30.5 was used. The microstructures were recorded using bright-field (BF) imaging and extended depth-of-focus corrections.

For the scanning electron microscopy (SEM) analysis, the field emission Hitachi S4800 was used. The samples were carbon coated to reduce electrostatic charging effects. A working distance of 8.8 mm was used with an acceleration voltage of 20 keV and a probe current of 10

μA with an equipped electron dispersive X-ray spectroscopy (EDS) detector. The SEM–EDS analysis used the quantitative ZAF correction technique.

Samples for transmission electron microscopy (TEM) analysis were extracted from metallic foil–fiber coating interfaces and baseline fiber coatings. To prepare for TEM analysis, the cold-mounted samples were milled into thin foils using a Ga^{+}-focused ion beam (FIB), Hitachi NB5000. The energy of the Ga^{+} ions progressively decreased from 30 to 5 keV to create the thin foils with approximate dimensions 3000 × 6000 × 50 nm. The thin foils were welded onto molybdenum grids and stored in a Ted Pella vacuum chamber. Molybdenum grids were used instead of standard copper grids to mitigate potential florescence effects from the grids during analysis.

For the TEM analysis, a field emission Talos F200X was used with an acceleration voltage of 200 kV and a probe current of ~ 1000 pA with an equipped EDS detector. Scanning transmission electron microscope images of the BF, dark field (DF), and high-angle annular DF (HAADF) were collected at angles of 9, 12 to 20, and 61 to 200 mrad, respectively. The TEM–EDS analysis was performed using a standardless semi-quantitative analysis on Bruker ESPRIT 1.9 software that used Cliff–Lorimer corrections. Every EDS spectrum and line scan were taken at three locations on the sample with three repetitions at each location to improve statistical significance. The EDS line scans plotted below represent the average of the three-line scans taken across each interface with errors bars representing the range of the collected data equally spaced for visual clarity.

III. RESULTS

A. *Baseline Samples*

As mentioned earlier, the optical fibers were examined before embedding. The baseline copper-coated fiber and the baseline gold-coated fiber were imaged, and their elemental compositions were quantified. The EDS spectra for the coatings were taken in high-magnification windows encompassing solely the metal coating. The images and EDS spectra are shown below in Figure 2. The arrows in Figure 2(a) show the slight charging effects present in the image. Figure 2(a) shows

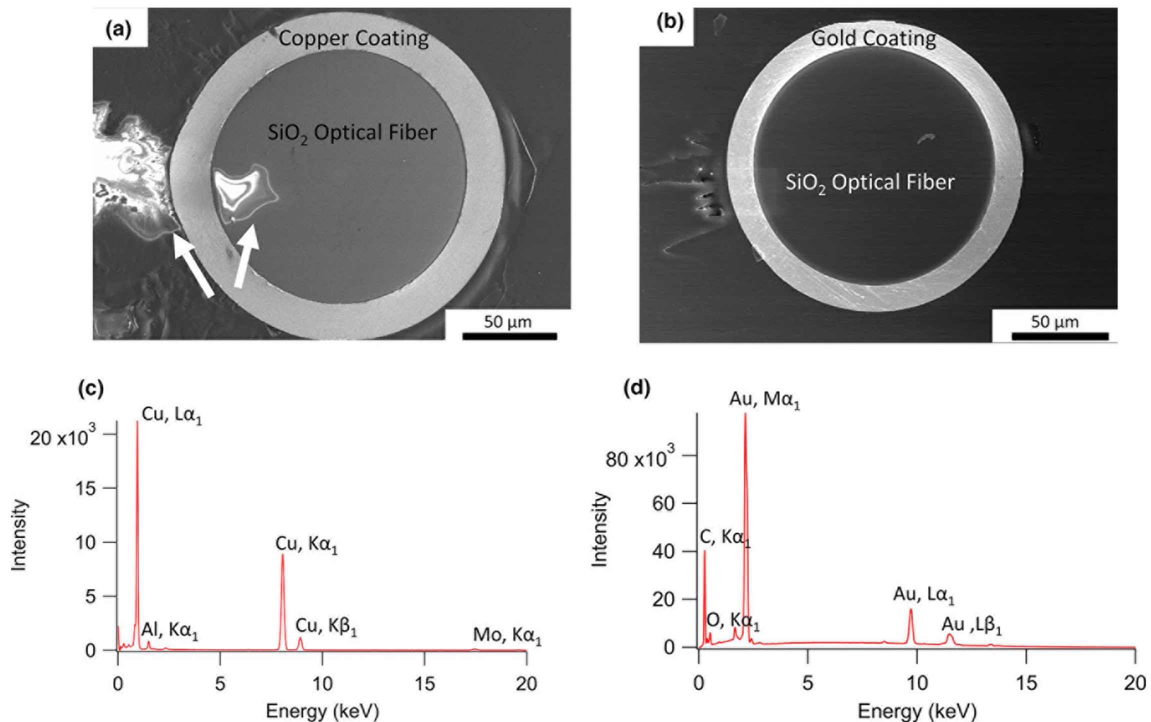

Fig. 2—Baseline-coated fiber images and EDS scans. (*a*) SEM image of copper-coated fiber, (*b*) SEM image of gold-coated fiber, (*c*) TEM–EDS spectrum of copper-coated fiber, and (*d*) SEM–EDS spectrum of gold-coated fiber.

Table I. TEM–EDS Results of Baseline Copper-Coated Fiber

Element	Carbon	Oxygen	Aluminum	Silicon	Copper	Molybdenum
At. Pct	7.2	2.1	4.5	0.1	86.1	0

the copper-coated optical fiber, and its corresponding EDS spectrum is shown in Figure 2(c). Figure 2(b) shows the gold-coated optical fiber, and its corresponding EDS spectrum is shown in Figure 2(d). From the SEM image of the baseline copper sample, the cross-sectional area of the electroplated copper is 9110 μm^2.

The EDS spectra were analyzed using the procedure described in Section II–C to create the elemental composition results, as shown in Tables I and II. To perform the TEM–EDS characterization of the baseline copper-coated fiber (Table I), the FIB sample was welded to a molybdenum grid. Although molybdenum appears in the EDS spectrum, the elemental composition deconvoluted the contribution of the molybdenum to the overall composition. This resulted in the copper-coated baseline fiber having a majority of copper with approximately 4.5 at. pct aluminum impurity. In the SEM–EDS characterization of the baseline gold-coated fiber (Table II), the carbon and oxygen found in the spectrum were also deconvoluted from the elemental composition. This resulted in the gold-coated sample having 100 pct gold.

Table II. SEM–EDS Results of Baseline Gold-Coated Fiber

Element	Carbon	Oxygen	Gold
At. Pct	0	0	100

B. *Bi-layer Interfaces*

This section describes the results pertaining to the *bi-layer interface* between the two different metals. The Al-Cu sample was examined at two different interface locations, and the Ni-Au sample was examined at one interface location. Two different interface locations of the Al-Cu sample were analyzed because the interfaces appeared significantly different with an open boundary (*i.e.*, not good joint) appearing in the first Al-Cu interface and a tight boundary (*i.e.*, good joint) appearing in the second Al-Cu interface. Since the focus of this paper is related to interdiffusion across the interfaces that have been joined, the analysis primarily focused on the tight boundaries including the second Al-Cu interface and the Ni-Au interface. The data from the 2nd Al-Cu interface are also used in the diffusion calculations to be described later. Once the calculations are calibrated for these conditions, these calculations were extended to other interfaces to obtain the final diffusivity and vacancy concentration values.

The first Al-Cu interface is shown in Figure 3. Figures 3(a) and (b) show an optical micrograph and SEM overview of the embedded metallized optical fiber. The aluminum foil, copper coating, and SiO_2 optical fiber are shown. The halo (indicated by an arrow in Figure 3(b)) is caused by charging effects in the electron microscope. Figures 3(c) through (e) show high-magnification TEM images of the interface between the copper and aluminum. There are many nano-scale voids, porosities, and open spaces between the two metals, as indicated by the circles in Figures 3(c) through (e). From the TEM images, the interface region is roughly 250 nm wide. From the SEM image of the embedded electroplated copper, the cross-sectional area is 9878 ± 17 μm^2.

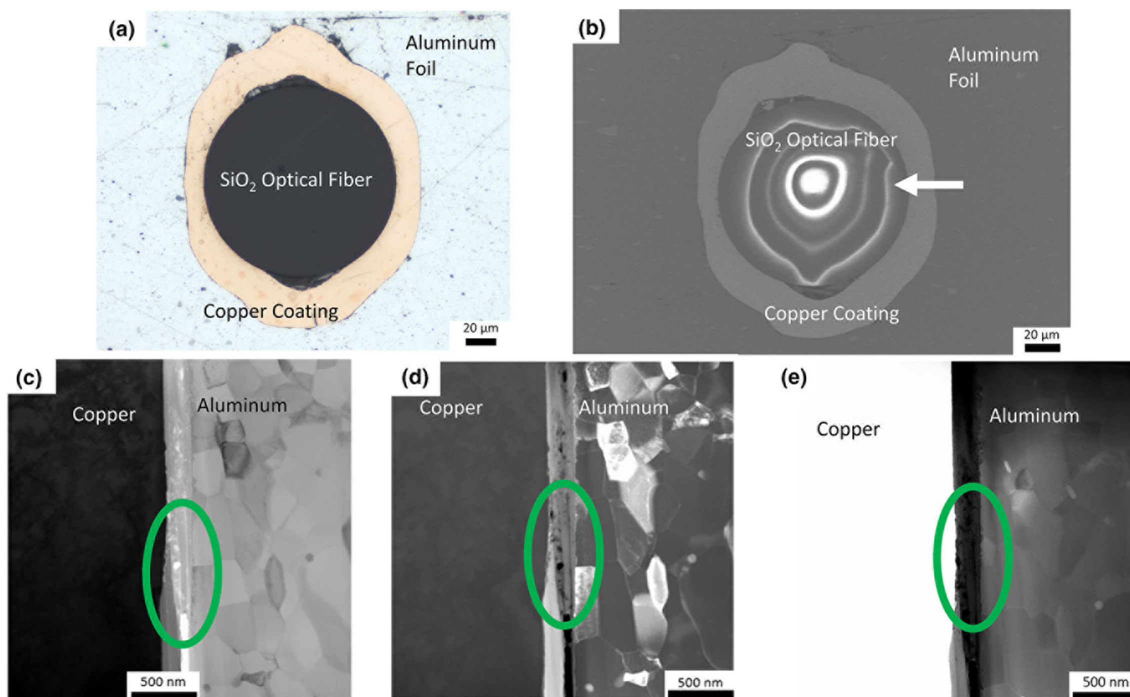

Fig. 3—First Al-Cu interface images: (*a*) optical, (*b*) SEM, (*c*) BF, (*d*) DF, and (*e*) HAADF. The interface is normal to the beam direction.

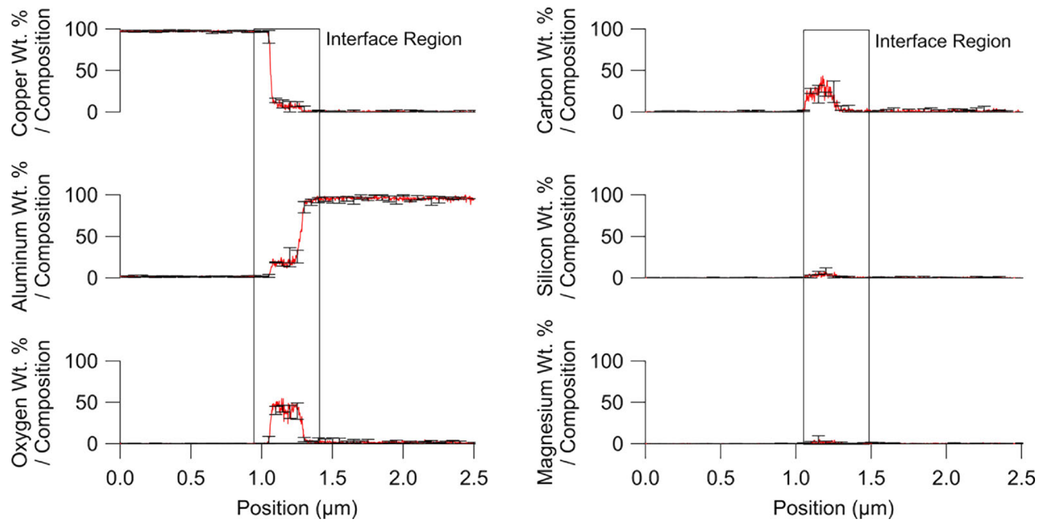

Fig. 4—TEM–EDS line-scan profiles of the first Al-Cu interface.

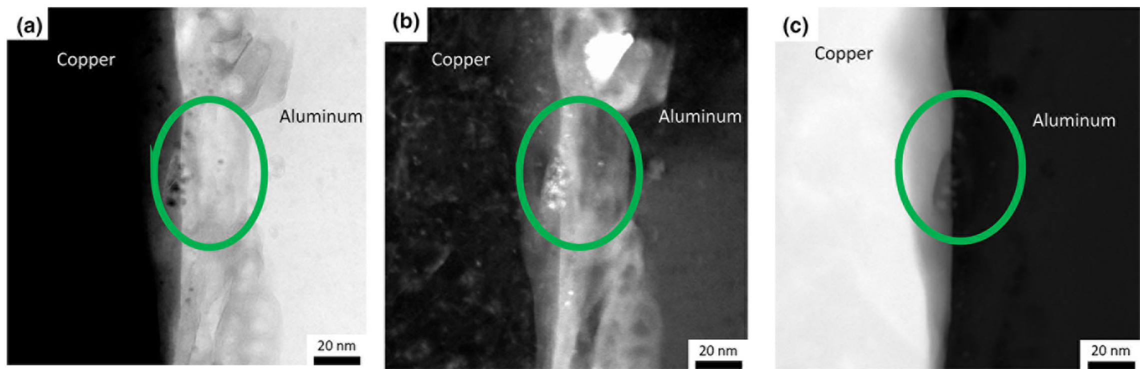

Fig. 5—Second Al-Cu interface images: (*a*) BF, (*b*) DF, and (*c*) HAADF. The interface is normal to the beam direction.

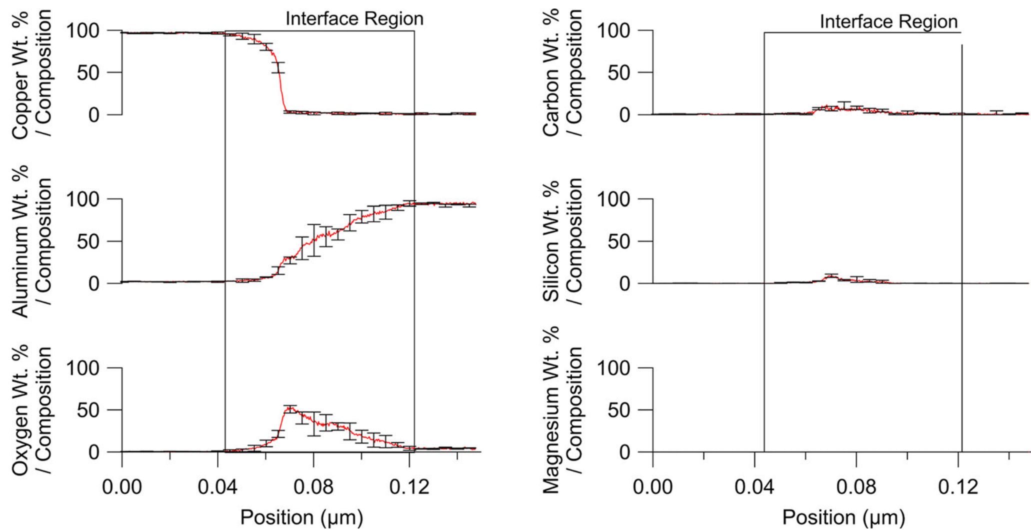

Fig. 6—TEM–EDS line-scan profile of the second Al-Cu interface.

The elemental concentration variation across the first Al-Cu interface is shown in Figure 4. Copper, aluminum, oxygen, carbon, silicon, and magnesium are shown. The interface region between the copper and the aluminum region is highlighted. Large amounts of oxygen and carbon are present in this region, as well

as minor amounts of silicon and magnesium. From the TEM–EDS data, the interface region is concluded to be approximately 300 nm wide.

The second Al-Cu interface is shown in Figure 5. The high-magnification TEM images shown in Figure 5 are from the same original sample shown in Figures 3(a) and (b); thus, the optical micrograph and SEM overview images are not repeated in Figure 5. The highlighted circles indicate the part of the interface region between the metals. Although some open regions could exist, there are fewer voids, porosities, and open regions than in the first Al-Cu interface (Figure 3). From the TEM images, there appears to be some type of intermixing between the aluminum and copper in this region. This region is measured to be ~ 40 nm wide.

The elemental spectrum across the second Al-Cu interface is shown in Figure 6. Copper, aluminum, oxygen, carbon, silicon, and magnesium are shown. The interface region between the copper and the aluminum region is highlighted. The interface region of the second Al-Cu interface (Figures 5 and 6) is significantly different than first Al-Cu interface (Figures 3 and 4). In the second interface region, a combination of copper, aluminum, and oxygen comprise the majority of the interface region. Other elements—such as carbon, silicon, and magnesium—comprise nearly insignificant portions of the interface. Over half the interface region is a combination of aluminum and oxygen, suggesting that an aluminum oxide is present. From the TEM–EDS data, the interface region is measured to be ~ 70 nm wide.

The Ni-Au interface images are shown in Figure 7. Figures 7(a) and (b) show an optical micrograph and SEM overview of the embedded metallized optical fiber. The nickel foil, gold coating, and SiO_2 fiber are shown. The particles indicated by the arrow in Figure 7(b) could be from carbon particles deposited onto the SEM surface to reduce charging effects. The particles could also be impurities caught in the open region between the coating and the film before imaging that escaped during the microscopy vacuum process. Figures 7(c) through (e) show the high-magnification TEM images of the interface between the gold and nickel. The interface between the two metals is highlighted with circles. From the TEM images, the interface region is roughly 40 nm wide. Additionally, there is a small void on the left side of the highlighted gold-nickel interface seen in the TEM images. This void appears bright in the BF image in Figure 7(c) and dark in the HAADF image in Figure 7(e). The SEM image of Figure 7(b) has gold coating in the upper right corner, but the optical image of Figure 7(a) does not. Although the samples are the same, the optical image was taken after re-polishing after the FIB–TEM sample preparation, resulting in an optical image roughly 20 μm below the surface of the SEM image.

The elemental spectrum across the Ni-Au interface is shown in Figure 8. Gold, nickel, iron, aluminum, and oxygen are shown. The interface region between the gold and nickel region is highlighted. In this interface region, gold and nickel are present simultaneously with very minor contributions by other elements, such as iron, aluminum, and oxygen. Since gold and nickel are immiscible metals, the presence of both metals in the same region is very surprising and unusual. From the

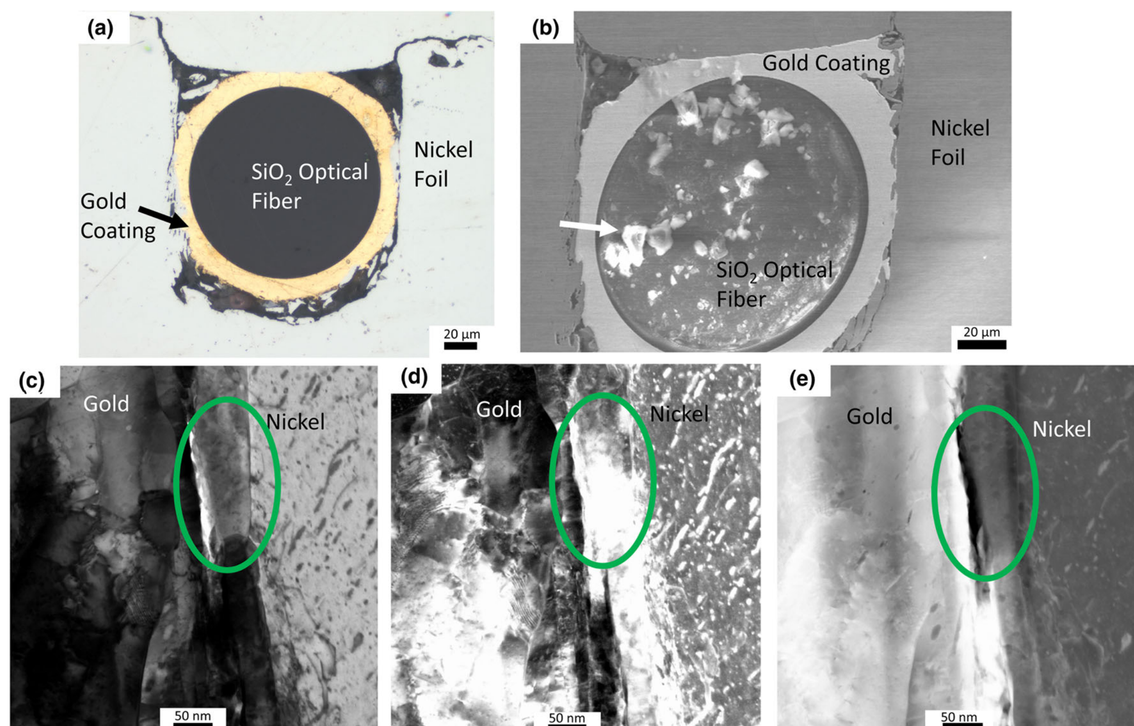

Fig. 7—Ni-Au interface images: (*a*) optical, (*b*) SEM, (*c*) BF, (*d*) DF and (*e*) HAADF. The interface is normal to the beam direction.

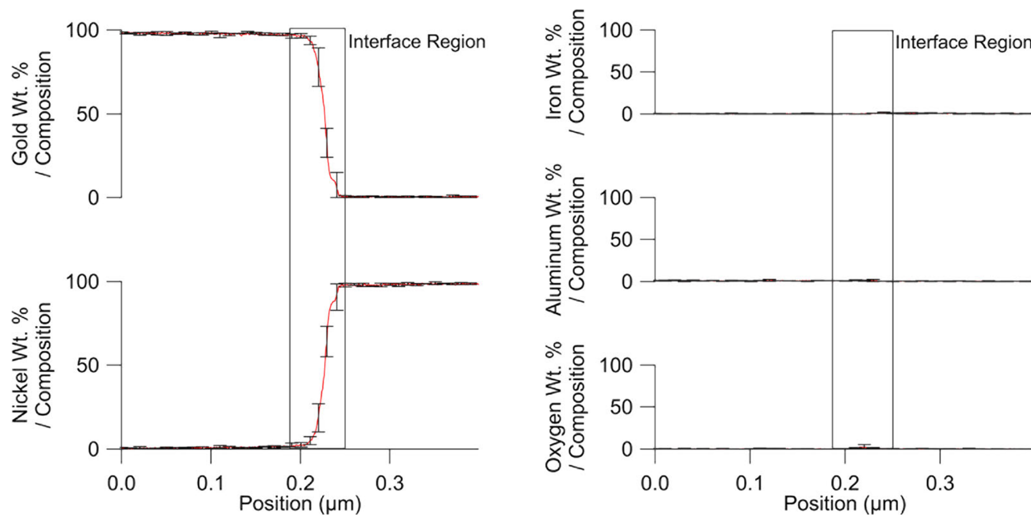

Fig. 8—TEM–EDS line-scan profiles of the Ni-Au interface.

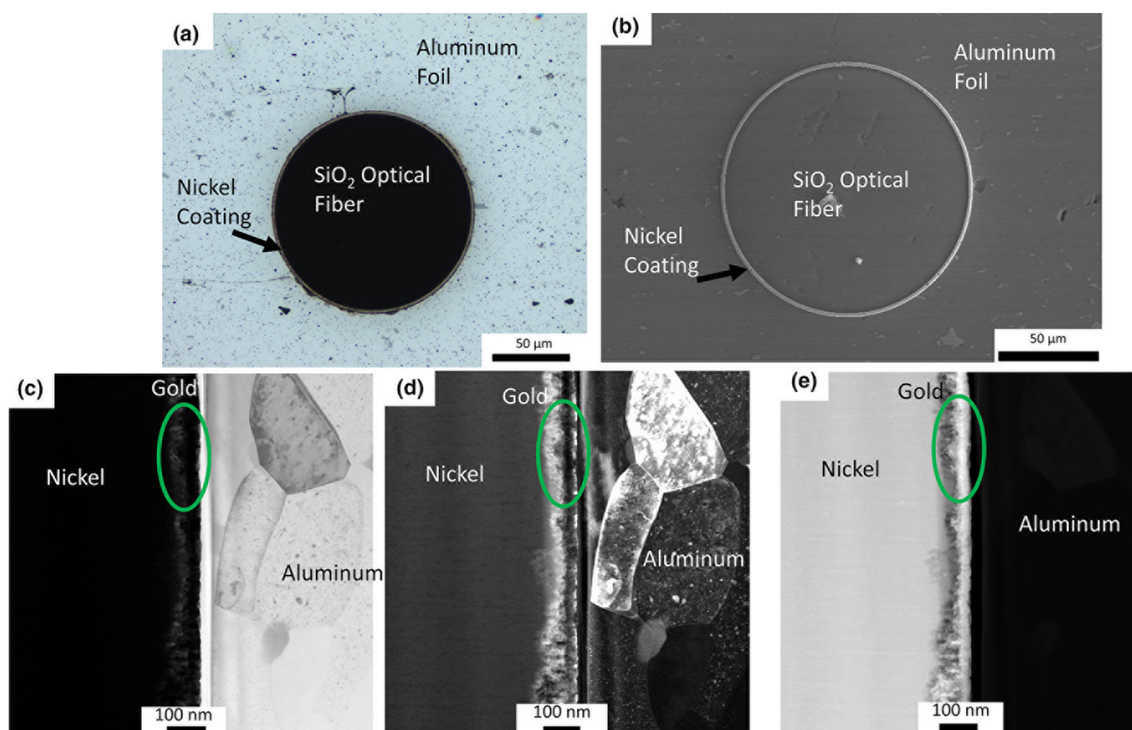

Fig. 9—Al-Au-Ni interface images: (*a*) optical, (*b*) SEM, (*c*) BF, (*d*) DF, and (*e*) HAADF. The interface is normal to the beam direction.

TEM–EDS data, the interface region is measured to be ~ 50 nm wide.

C. *Tri-layer Interfaces*

The *tri-layer interface* across three different metals was explored in the Al-Au-Ni sample, as shown in Figures 9 and 10. The Al-Au-Ni interface images are shown in Figure 9. Figures 9(a) and (b) show an optical micrograph and SEM overview of the embedded metallized optical fiber. The aluminum foil, nickel coating, and optical fiber are shown in these overview images. The gold monolayer is not apparent in these low-magnification images. Figures 9(c) through (e) show the high-magnification TEM images of the tri-layer interface. The nickel is on the left, the aluminum is on the right, and the gold monolayer is in the middle. This small gold layer is highlighted with circles. From the TEM images, the width of the gold monolayer is measured to be 90 nm wide.

Figure 10 shows the elemental spectrum across the Al-Au-Ni interface. Nickel, gold, aluminum, oxygen, and phosphorous are shown in this highlighted interface. The gold monolayer between the nickel and

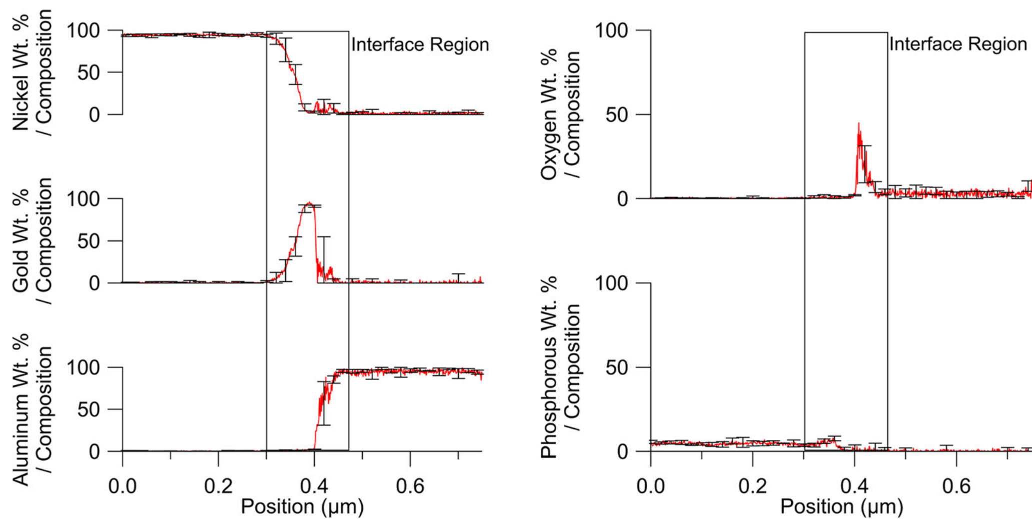

Fig. 10—TEM–EDS line-scan profiles of the Al-Au-Ni interface.

aluminum can be clearly seen. There is a relatively broad boundary interface between the nickel and the gold and a relatively sharp boundary interface between the gold and the aluminum UAM foil. Additionally, there is a significant rise in oxygen content on the aluminum side of the interface, which suggests that an aluminum oxide combination could be present at that interface. According to the TEM–EDS data, the interface region of the nickel and gold is ~ 90 nm wide, and the interface between the gold and the aluminum foil is less than ~ 5 nm wide.

D. *Measured Solute Diffusion*

In Figure 10, the total interface distance between the gold monolayer and the aluminum foil is less than ~ 5 nm, which is near the resolvable limit of the TEM–EDS analysis after considering beam broadening effects and possible slight tilting and twisting of the interface relative to the incident electron beam. Therefore, the gold monolayer on the outside of the nickel-coated fiber could have prevented any significant interdiffusion in the tri-layer Al-Au-Ni sample. Figures 4, 6, and 8 show that there is interdiffusion across the bi-layer metal interface after the UAM embedding process.

To quantitatively interpret interdiffusion across the bi-layer interfaces, a time and temperature profile that the samples experienced must be estimated, although it was not directly measured in this study. The temperature profile during ultrasonic consolidation (UC) can be affected by several factors including power from the sonotrode, normal force, metal–metal contact area, sonotrode speed, and oscillation frequency. The temperature contribution from these factors has been experimentally measured during UAM bonding[16,17] and ultrasonic spot welding, USW[18–22] using type K thermocouples and thermal imaging cameras. A term of energy per unit area (J/mm^2) is typically used to normalize the UC welding parameters.

Using a simple derivation described by Sriraman *et al.*,[17] the energy per unit area experienced by the samples in this study is 10 to 16 J/mm^2, which according to previous studies[16–22] corresponds to a peak temperature between 115 °C and 400 °C. The oscillation amplitude and frequency could also adjust the mean temperature value by 20 °C,[16] although these are relatively minor factors compared to the 285 °C temperature variation found throughout literature. The large range of the potential peak temperatures is strongly affected by the large experimental errors which exist in UAM temperature measurements. As mentioned above, the applied ultrasonic frequency is 20 kHz. Therefore, the time resolution required to accurately measure temperature from each back-and-forth pass of the sonotrode must be below 0.05 ms (1/20 kHz).

UAM thermal measurement studies have recognized this and maximized their thermocouple sampling rate to 10,000/s while using an unsheathed 70 μm diameter Type K thermocouple to minimize the thermocouple time constant. This corresponds to receiving a signal from the thermocouple every 0.1 ms.[16,17] The time constant of the thermocouple should also be considered. The time constant is the time required for the sensor to respond to at least 63.2 pct of its total output signal when subjected to a step change in temperature. This is a function of the thermal heat capacity and mass of the thermocouple.[47–49] For an unsheathed 70 μm Type K thermocouple at room temperature, the time constant is approximately 135 to 150 ms.[50–53] This means although a rapid signal was recorded from the thermocouple every 0.1 ms, the thermocouple could only respond to temperature changes at most every 135 ms. Therefore, the true magnitude of the temperature spike due to UAM bonding could be missed while using these thermocouples. Additionally, the non-contact thermal imaging cameras used in the above studies cannot access a direct line of site with the internal weld, and the emissivity of metals allows only a fraction of the radiative heat to be detected.[54]

Considering these factors of the UC normalization term, the previous experimental research, and the experimental uncertainty of the temperature

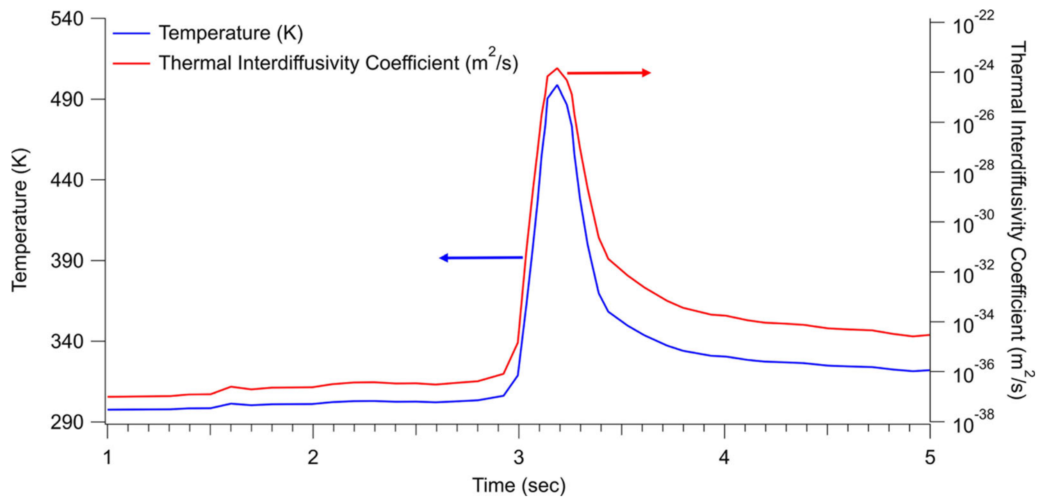

Fig. 11—Estimated thermal profile from Sriraman *et al.*[16] and interdiffusion coefficient assuming only thermal contributions.

measurements, an approximate peak temperature value of 225 °C (498 K) is assumed for the diffusivity calculations below. Using the arbitrary temperature profile from Sriraman *et al.*[16] and this approximate peak temperature, an estimated thermal profile can be created for the welding parameters used in this study. This is shown in Figure 11. The estimated thermal profile is used since no temperature measurements were taken in this experiment.

Additionally, the phenomenological equation for thermal interdiffusivity $\tilde{D}$ between aluminum and copper, derived by Matsuno and Oikawa[55] using the Boltzmann–Matano method, can be considered here. The interdiffusivity across the temperature profile in Figure 11 can be calculated using the values of atomic fraction of aluminum in copper N_{Al} from the baseline copper fiber (~ 4.5 at. pct) and the gas constant R of 8.314 J/(K mole). Also note that the term $\tilde{D}$ simply denotes interdiffusivity between an A-B alloy, while the term D typically denotes diffusivity of a sole solute atom in an otherwise homogenous solid solvent solution. The former is considered in this study.

$$\tilde{D}(N_{\mathrm{Al}}) = 0.43 \times 10^{-4} \cdot \exp\left\{-\frac{(194,000 - 180,000 N_{\mathrm{Al}})}{RT}\right\}. \quad [1]$$

The method commonly used for determining any diffusivity during heating up and cooling down time is considered. In this case, the solution for the diffusivity for each time t interval is replaced by the averaged product $\bar{D}t$ by the equation $\bar{D}t = \int_0^t D(t)\mathrm{d}t$.[56] Using this method the interdiffusivity during the interface temperature profile, also shown below in Figure 11, demonstrates the heating up and cooling down time providing a negligible contribution to the total time-integrated interdiffusivity. Therefore, only the time (0.2 seconds) at peak temperature will be used for the experimental diffusivity equations below.

Considering the diffusion couple profile method[56,57] from the second Al-Cu interface shown in Figure 6, the distance, x, at which the aluminum concentration reaches 50 pct of the maximum aluminum concentration is 0.035 μm from the edge of the interface. Using Fick's second law approximation, the experimental interdiffusivity during a time interval of 0.2 seconds is 6.1×10^{-15} m^2/s.

$$x \sim \sqrt{\tilde{D}t}. \quad [2]$$

Significant discrepancy is found when comparing between the expected interdiffusivity value from the thermal approach by Matsuno *et al.* and the experimentally estimated interdiffusivity value from the EDS measurements of solute diffusion (10^{-24} vs 10^{-15} m^2/s, respectively). The small residence time and minimal homologous temperature rise (~ 0.4 T/T_{m}) prevent thermal equilibrium diffusion from being a viable explanation of the observed atomic motion (roughly 9 orders of magnitude discrepancy). Thus, alternative diffusion mechanisms must be operational.

Finally, it should be noted that the energy normalizing term (J/mm^2) could be an incomplete description for the thermal profile experienced at the interfaces in this study due to the unique geometries present. The thermal profiles were created for UAM *foil–foil* bonding in which each foil has the same ratio of cross-sectional area of 1:1, whereas the present experiment investigated the *foil–fiber coating* interface where the cross-sectional area between the two bonded geometries is not equal. In fact, using the foil width of 25.4 mm, foil thickness of 0.15 mm, and the electroplated copper cross-sectional area of 9110 μm^2, the ratio of the foil–fiber coating cross-sectional area is 1:0.0024. It is possible the disproportional geometries create a unique situation unlike what would be observed with two equally proportional geometries. Further analysis is needed to determine the potential impact of this unequal cross-sectional area.

IV. DISCUSSION

A. *Rationalization of the Interdiffusion*

The phenomenological approach to diffusion using Fick's laws and thermal equilibrium diffusion, as described above, clearly does not provide a complete description of the atomic motion during UAM. Therefore, the atomistic approach to diffusion can be considered. The interdiffusion equation is shown below where f is the correlation factor, a_0 is the lattice constant, v is the Debye frequency of atomic vibration on its lattice site, E_m is the vacancy migration energy, k is the Boltzmann constant of 8.617×10^{-5} eV/K, and T is the absolute temperature.[56–62] For the dissimilar FCC metal interfaces explored here, in which the vacancy–atom exchange ratio is not known, a nominal value of 0.78 is used for the correlation factor.[63–70]

$$\tilde{D} = f{a_o}^2 X_v v \cdot \exp\left(-\frac{E_m}{kT}\right). \qquad [3]$$

The material constants that are needed to obtain the interdiffusion coefficients from Eq. [3] for the elemental concentration profiles of the Al-Cu interfaces and the Ni-Au interface are shown in Table III.

Using the material constants for copper and gold shown in Table III, the vacancy concentration needed for interdiffusion across each interface can be calculated. Table IV shows the values for each interface and the calculated interdiffusivity using Fick's second law approximation.

To illustrate the magnitude of the elevated vacancy concentrations estimated in Table IV, thermal equilibrium vacancy concentrations can be calculated as shown below in Table V for the estimated thermal profile maximum and the melting temperature. If the vacancy concentration corresponds to thermodynamic equilibrium at a given temperature, then it is determined by the vacancy formation energy E_f and the absolute temperature.[74–76]

$$X_v = \exp\left(-\frac{E_f}{kT}\right). \qquad [4]$$

This analysis demonstrates that the estimated vacancy concentrations across the sample interfaces necessary to explain the observed solute diffusion are quite large. The vacancy concentrations are much larger than thermal equilibrium levels at the estimated maximum temperature and even at the metals' respective melting temperatures. These values would be quite alarming if they are correct because they begin to reach the critical vacancy concentration hypothesized by Johnson[77] based on the defect-induced shear catastrophe.[78,79] This limit describes the lattice defect concentrations that are required to raise a metallic material's free energy to the point that it loses its crystallinity and becomes amorphous. Other examples of a material briefly losing its crystallinity include irradiation damage cascades[80–83] and ARB mechanical alloying, as mentioned below. However, as mentioned previously, there are various measurement uncertainties and alternative possibilities beyond just an elevated vacancy concentration that could explain the interdiffusion. Therefore, these vacancy concentration values should be considered as upper bounds rather than exact values.

The elemental concentrations in the various interfaces can be briefly compared. In the first Al-Cu interface (Figure 4), the main elements of aluminum and copper experienced interdiffusion, but non-trivial fractions of the minor solute atoms carbon, oxygen, and silicon were also observed in the open boundary interface. In contrast, in the second Al-Cu interface (Figure 6) only oxygen was observed as an interface impurity element. If an ordered crystal were created near this interface, a thin intermetallic of aluminum and copper and/or an aluminum oxide could have been present. Finally, the Ni-Au interface (Figure 8) appears to have nickel and gold present in the same region although the equilibrium phase diagram and thermodynamic assessments of this system suggest limited mutual miscibility at low temperatures.[84,85] This is surprising although the mechanical mixing of immiscible metals has also been found in other bonding processes, such as the ARB process, as discussed later.

The similarities and differences between the two Al-Cu interfaces should be discussed further. Both interfaces demonstrate the presence of voids and porosity as shown as white dots in the BF images in Figures 3(c) and 5(a), and black dots in the DF images in Figures 3(d) and 5(b). It is hypothesized that these voids resulted from the accumulation of vacancies migrating towards the interfaces. Clearly, the main difference between the two interfaces is the presence of the ellipsoidal gap between the metals. The first Al-Cu interface in Figure 3 has a ~ 100 nm gap between the Al and Cu, while the second Al-Cu interface in Figure 5 does not have a gap between the metals. Since solutes are observed on opposite sides of the gap in Figure 3, it is believed that the Al and Cu likely separated after interdiffusion of these elements. The subtle difference between the interfaces is attributed to non-uniform thermo-mechanical conditions at the interface during

Table III. Material Constants for Interdiffusion Expression

Material	E_m (eV)[71]	v (s^{-1})[72]	a_0 (Å)[73]
Copper	0.70	7.98×10^{13}	3.6
Gold	0.71	4.92×10^{13}	4.1

Table IV. Interdiffusivity and Vacancy Concentration of Each Interface

Sample	$\tilde{D}$(m^2/s)	X_v (Atomic Fraction)
First Al-Cu Interface	5.0×10^{-14}	7.5×10^{-2}
Second Al-Cu Interface	6.1×10^{-15}	9.2×10^{-3}
Ni-Au Interface	3.1×10^{-15}	7.4×10^{-3}

Table V. Thermal Equilibrium Vacancy Concentrations

Material	E_f (eV)[71]	T_m (K)	X_v (Atomic Fraction) at 225 °C	X_v (Atomic Fraction) at T_m
Copper	1.28	1358	1.12×10^{-13}	1.78×10^{-5}
Gold	0.93	1337	3.90×10^{-10}	3.13×10^{-4}

the ultrasonic metal welding process.[86] This is expected to result in non-uniform distribution of plastic strains.[87] As a result, some of the interfaces that had joined may be torn apart with the high magnitude of plastic strain (*e.g.*, 1st Al-Cu interface, Figure 3) while others remained intact (2nd Al-Cu interface, Figure 5). It is important to note that any solid-state or resistance spot welding geometries exhibit non-uniform stress distribution due to the inherent geometry effects.[88]

The interdiffusion physics described above uses the entire interface width including the gap. Since the first Al-Cu interface has a gap in the middle of the interface region, the total distance used for the interdiffusion equation is larger than it otherwise would be. This creates an even larger vacancy concentration as shown in Table IV. The second Al-Cu interface did not exhibit separation; therefore, it was chosen to illustrate the interdiffusion physics due to the absence of the potentially convoluting gap.

From an atomistic point of view, the mobility of large solute atoms (Al, Cu, Ni, Au) require vacancies to be present since their movement depends on the substitutional diffusion mechanism (*i.e.*, there must be an open lattice location for a solute atom to jump into).[63,74,89] However, the mobility of A and B atoms in an A–B metal interface is typically not equal, as Kirkendall's experiments have demonstrated.[60,61] As hinted at earlier, the interdiffusion is typically compositionally dependent, although a simplified interface interdiffusion value was created to demonstrate the physics present in this study.

Although major solute atoms require vacancy point defects to migrate, traditional interstitial impurity atoms (C, O) do not require vacancies to migrate. This simpler migration pattern is described as interstitial diffusion (in contrast to substitutional diffusion) in which the impurity solute atoms, being much smaller in atomic diameter than the bulk solvent atomic diameter, diffuse from one interstitial site to another. In the FCC matrix, these are the octahedral and tetragonal lattice sites in between the host FCC lattice.[63,74,89] The large mobility of the oxygen atoms migrating towards the interface in the Al-Cu system is likely due to this interstitial diffusion mechanism. This mechanism can also help describe the small atom dispersion that others have observed in UAM interfaces.[38] Although carbon is often described as an interstitial atom for typical metals such as BCC iron,[63,74,89] carbon has extremely low solubility in aluminum, typically less than 0.1 ppm at and below 750 °C.[90–93] This makes the detected carbon X-rays shown in Figure 3 quite curious. Since the TEM–EDS in this study used a field emission electron source in an ultra-high vacuum, the carbon X-rays have likely originated directly from the sample. Further research including atom probe tomography is needed to understand the mechanisms.

For a complete understanding of the defect physics, vacancy migration must be considered in addition to the major and minor solute migration. Consider first that when bonding was initiated, there were two atomically clean planes of atoms in contact. Then due to the elevated vacancy concentration, there was a flux of atoms outward from this flat plane towards the opposite bulk region. This created an interface region 50 nm or more. For this outward flux of atoms to occur (from the initially clean interface towards the bulk), there must also have been an inward flux of vacancies to support it (from the bulk towards the center of the interface region).

Although this flux of vacancies and solute atoms could have occurred solely through the bulk lattice, the material was not a single crystal. Although detailed electron backscatter diffraction (EBSD) analysis, for microstructural characteristics, was not performed in these samples due to limited size, many other UAM interface analyses have shown elevated dislocation densities, severe grain refinement, large concentrations of high-angle grain boundaries (HAGB), and migrating grain boundaries towards the foil interfaces likely due to a process analogous to dynamic recrystallization, DRX.[10,15–17,34,36,94–99] During the DRX process, a crystal releases internal stored energy from accumulated plastic strains. New essentially strain-free crystals grow at the expense of the deformed crystals. The material is swept by HAGB, perhaps more than once, as the material realigns atoms into crystals with lower free energy.[74,100,101] Some have postulated that the migrating grain boundaries not only sweep through each side of a UAM foil interface, but even across foil interface boundaries.[11] Nevertheless, this phenomenon is less likely with dissimilar foil interfaces due to the decreased grain boundary mobility while carrying solute atoms.[100,102]

Although sweeping grain boundaries may not rapidly carry solute atoms, stationary grain boundaries could offer short circuit solute diffusion pathways in addition to or instead of vacancies.[63] Grain boundary diffusion of vacancies and interstitials occurs primarily through the relatively open space between grains. The defects migrate by jumping from the lattice, into the grain boundary, traveling through the grain boundary, then jumping back out into the lattice. Both vacancies and interstitials can move in grain boundaries with single atom exchanges or with collective jumps, although most often the motion involves two or more atoms. There is no clear consensus on the relative strength of the

different types of point defects on grain boundary diffusion in metals, but there is clear evidence that both contribute to the diffusivity.[63,100,103–105] Of course, if grain boundary interdiffusion significantly contributes to the major solute interdiffusion in this study, then the vacancy concentration required for the interdiffusion, as predicted in Table IV, could be lower than estimated.

B. *Critique of Previous UAM Enhanced Vacancy Concentration Analyses*

As shown in Table IV, the atomic fraction of vacancies across the three different interdiffusion boundaries is on the order of 10^{-3}, although as discussed, grain boundary interdiffusion could contribute to lowering this value. This extreme vacancy concentration is still several orders of magnitude lower than the vacancy concentration of 10^{-1} proposed by Gunduz *et al.* Several factors could have caused the significant difference between these vacancy concentrations. Gunduz *et al.* did not consider the classical random walk diffusion physics,[56–62] nor did Gunduz *et al.* consider any thermal cycles or temperature increases. In fact, the published literatures show that the temperature increase at the interface is significant.[16–22,41,86]

In addition to the defect physics and temperature profiles overlooked by Gunduz *et al.*, the initial argument of their paper was based on experimental data that did not mention or consider measurement uncertainties. The author's initial argument was based on a single SEM–EDS line profile with a 1 μm range of compositionally equivalent material, which the author claims became molten. They did not consider the SEM operating parameters nor the interaction volume convolution,[106,107] which is larger than the lateral range of the supposed molten materials. The issues outlined above signify that the Gunduz *et al.* conclusions may not be accurate.

C. *Correlation of the Interdiffusion Observed in ARB Processing*

The UAM process is not the only process that can create layered materials driven far from equilibrium. The ARB process can create mechanical alloying of immiscible materials due to SPD, which refines the microstructure as dislocations interact during the repeated severe straining process.[40,108] The mechanical alloying of different materials has experimentally been found to create layered foils such as aluminum and magnesium with high diffusivities and intermetallic formation.[109,110] Copper and zirconium have also experienced mechanical alloying with amorphization, which is experimentally observed in extreme cases.[111]

The fundamental phenomena causing deformation induced mechanical and chemical mixing from phases that have non-soluble elements is still debated. The common explanations for this mixing include a purely diffusion-driven mechanism, defect-enhanced diffusion, mechanical mixing (also referred to as shuffling or ballistic mixing), and deformation-driven amorphization.[112]

D. *Postulation Regarding the Vacancy Formation*

This work explored the elemental composition profiles across bi-layer metal boundaries and calculated interdiffusivity values across the interfaces that must exist according to the measured data. These interdiffusivity values were rationalized using vacancy concentrations that are several orders of magnitude above thermal equilibrium values. The exact origin of these vacancies is still uncertain and should be explored further.

Introduction of defects such as vacancies increases with applied plastic deformation. There are several methods for describing plastic deformation from externally applied work. A common method for comparing the work done to a metal through traditional cold roll bonding or the ARB process is a reduction of thickness measurement. Typical values for roll bonding processes are ~ 30 to 70 pct reduction of thickness.[113–117] Comparing the cross-sectional area of the electroplated copper before and after the embedding process demonstrates a negligible − 3.2 pct reduction of thickness. Therefore, only a minor reduction of thickness occurred during the ultrasonic bonding process although a significant number of vacancies were apparently still created.

Additionally, strain measurements were being investigated when the copper-coated fiber and the nickel-coated fiber were embedded into aluminum. These measurements could help in providing insight into the nature of the vacancy formation. The strain across the fiber was measured before and after the embedding process. The difference between these strain measurements is called the *residual strain* in the fiber. Petrie *et al.* performed these measurements,[26] which are shown in Figures 12 and 13. These strains are calculated based on the difference between the optical transmission scans of the fiber before embedding and after embedding. Both the Al-Cu sample and the Al-Au-Ni sample showed significant residual compressive strain. The strain could be related to the enhanced interdiffusivity calculated, elevated vacancy formation, and dynamic recrystallization. However, as mentioned above, the lack of elemental distribution in the Al-Au-Ni sample is likely due to the gold deposited during the nickel coating procedure. In addition, caution must be taken on interpretation of the differences in the magnitude of the strain due to complexities based on variables relevant to ultrasonic additive manufacturing, *i.e.*, channel depth, load profile, and fixturing conditions.

Finally, it should be noted that some researchers have postulated that elevated vacancy concentrations could be created directly from ultrasonic energy introduced into a material.[118] The theories have proposed that the ultrasonic energy could be unpinning dislocations, and vacancies could be created as the dislocations jog in a non-conservative manner.[119] Although studies have pointed towards observed increases in electrical resistivity during applied ultrasonic energy, which implies additional lattice defects,[120] critics have noted that temperature effects, which are non-trivial during applied ultrasonic frequencies (Section III–D and Eq. [4], were not considered in these analyses.

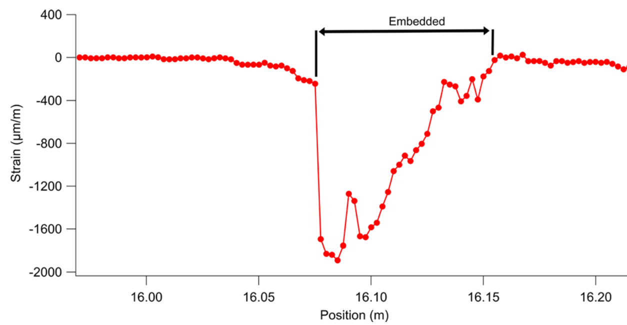

Fig. 12—Residual strain measurements in the Al-Cu sample. Used with permission from Ref. [24].

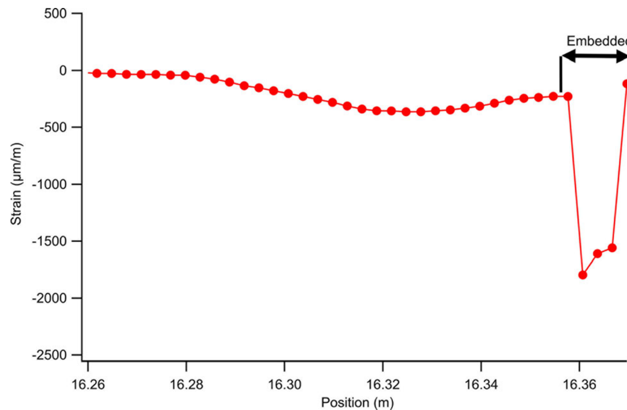

Fig. 13—Residual strain measurements in the Al-Au-Ni sample. Used with permission from Ref. [24].

V. SUMMARY AND CONCLUSIONS

The interdiffusion resulting from embedding metallized optical fibers in UAM foils was analyzed. Previous literature has rationalized UAM interface development in a variety of ways including a lack of temperature rise, a moderate temperature rise, bulk lattice diffusion, vacancy diffusion, grain boundary diffusion, and stationary or recrystallizing grain boundaries. Utilizing UAM specific power derivations, a temperature profile has been calculated, which is consistent with previous direct measurements. Although a mild temperature rise is present, it is not sufficient to rationalize the measured solute interdiffusion by thermal equilibrium diffusion processes. Instead, the solute diffusion levels are commensurate with transient vacancy supersaturation levels that are orders of magnitude higher than what can be explained based on a thermal equilibrium diffusion processes for the temperature profile associated with the UAM processes or by vacancy production associated with high strain rate deformation. The dynamic grain recrystallization process associated with UAM interfaces could also contribute to the atomic mobility. Postulated sources of the enhanced vacancy concentrations are briefly discussed. This work contributes to the understanding of solid-state bonding and the concurrent elemental interdiffusion based on existing solid-state defect physics knowledge.

ACKNOWLEDGMENTS

This research is sponsored by the Laboratory Directed Research and Development Program of Oak Ridge National Laboratory (ORNL), managed by UT-Battelle LLC, for the US Department of Energy. Adam Hehr and Mark Norfolk (Fabrisonic LLC, Columbus, Ohio) fabricated the embedded fiber samples. Dorothy Coffey assisted in TEM lamella fabrication. Metallography and optical microscopy were performed in the ORNL Manufacturing Demonstration Facility (MDF). SEM and EDS Bruker analysis were performed in the ORNL High Temperature Materials Laboratory (HTML). TEM was performed in the ORNL Low Activation Materials Development and Analysis Laboratory (LAMDA).

SUPPLEMENTARY INFORMATION

The online version of this article (https://doi.org/10.1007/s11661-020-06131-2) contains supplementary material, which is available to authorized users.

REFERENCES

1. C.M. Petrie, N. Sridharan, A. Hehr, M. Norfolk, and J. Sheridan: *Advanced Manufacturing and Material Science: General*, Springer, Cham, 2019, vol. 120, pp. 438–41.
2. D.R. White: *Adv. Mater. Process.*, 2003, vol. 161, pp. 64–65.
3. US 6,519,500 B1: United States Patent, 2003.
4. D.E. Schick: *Characterization of Aluminum 3003 Ultrasonic Additive Manufacturing*, Ohio State University, 2009.
5. R.F. Tylecote: *The Solid Phase Welding of Metals*, Edwards Arnold, London, 1968.
6. Fabrasonic: Ultrasonic additive manufacturing, https://www.youtube.com/watch?v=5s0J-7W4i6s. Accessed 1 Oct 2019.
7. R.J. Friel and R.A. Harris: *Procedia CIRP*, 2013, vol. 6, pp. 35–40.
8. H.T. Fujii, S. Shimizu, Y.S. Sato, and H. Kokawa: *Scripta Mater.*, 2017, vol. 135, pp. 125–29.
9. W.J. Sames, F.A. List, S. Pannala, R.R. Dehoff, and S.S. Babu: *Int. Mater. Rev.*, 2016, vol. 61, pp. 315–60.
10. R.R. Dehoff and S.S. Babu: *Acta Mater.*, 2010, vol. 58, pp. 4305–15.
11. M.R. Sriraman, S.S. Babu, and M. Short: *Scripta Mater.*, 2010, vol. 62, pp. 560–63.
12. T. Monaghan, A.J. Capel, S.D. Christie, R.A. Harris, and R.J. Friel: *Composites A*, 2015, vol. 76, pp. 181–93.
13. C. Petrie, N. Sridharan, C. Frederick, T. McFalls, S. Suresh Babu, A. Hehr, M. Norfolk, and J. Sheridan: *11th Nucl. Plant Instrum., Control. Hum.–Mach. Interface Technol. NPIC HMIT 2019*, 2019, pp. 459–68.
14. A. Hehr, M. Norfolk, J. Wenning, J. Sheridan, P. Leser, P. Leser, and J.A. Newman: *JOM*, 2018, vol. 70, pp. 315–20.
15. N. Sridharan, P. Wolcott, M. Dapino, and S.S. Babu: *Scripta Mater.*, 2016, vol. 117, pp. 1–5.
16. M.R. Sriraman, M. Gonser, H.T. Fujii, S.S. Babu, and M. Bloss: *J. Mater. Process. Technol.*, 2011, vol. 211, pp. 1650–57.
17. M.R. Sriraman, M. Gonser, D. Foster, H.T. Fujii, S.S. Babu, and M. Bloss: *Metall. Mater. Trans. B*, 2012, vol. 43B, pp. 133–44.
18. F. Haddadi and D. Tsivoulas: *Mater. Charact.*, 2016, vol. 118, pp. 340–51.
19. Y.C. Chen, D. Bakavos, A. Gholinia, and P.B. Prangnell: *Acta Mater.*, 2012, vol. 60, pp. 2816–28.

20. V.K. Patel, S.D. Bhole, and D.L. Chen: *Scripta Mater*., 2011, vol. 65, pp. 911–14.
21. A.A. Ward, M.R. French, D.N. Leonard, and Z.C. Cordero: *J. Mater. Process. Technol*., 2018, vol. 254, pp. 373–82.
22. H.T. Fujii, Y. Goto, Y.S. Sato, and H. Kokawa: *Scripta Mater*., 2016, vol. 116, pp. 135–38.
23. I.E. Gunduz, T. Ando, E. Shattuck, P.Y. Wong, and C.C. Doumanidis: *Scripta Mater*., 2005, vol. 52, pp. 939–43.
24. J.M. López-Higuera, L.R. Cobo, A.Q. Incera, and A. Cobo: *J. Light Technol*., 2011, vol. 29, pp. 587–608.
25. H.N. Li, D.S. Li, and G.B. Song: *Eng. Struct*., 2004, vol. 26, pp. 1647–57.
26. C.M. Petrie, N. Sridharan, M. Subramanian, A. Hehr, M. Norfolk, and J. Sheridan: *Smart Mater. Struct*., 2019, vol. 28, p. 055012.
27. A.D. Kersey: *IEICE Trans. Electron*., 2000, vol. 83, pp. 400–04.
28. T.K. Kragas, B.A. Williams, and G.A. Myers: *SPE Annu. Tech. Conf. Exhib*., 2001.
29. M.A.S. Zaghloul, A. Yan, R. Chen, M.J. Li, R. Flammang, M. Heibel, and K.P. Chen: *IEEE Trans. Nucl. Sci*., 2017, vol. 64, pp. 2569–77.
30. C.Y. Kong and R. Soar: *Appl. Opt*., 2005, vol. 44, p. 6325.
31. Y. Li, Z. Hua, F. Yan, and P. Gang: *Opt. Fiber Technol*., 2009, vol. 15, pp. 391–97.
32. D. Baudrand and J. Bengston: *Met. Finish*., 1995, vol. 93, pp. 55–57.
33. S. Shimizu, H.T. Fujii, Y.S. Sato, H. Kokawa, M.R. Sriraman, and S.S. Babu: *Acta Mater*., 2014, vol. 74, pp. 234–43.
34. N. Sridharan, M. Norfolk, and S.S. Babu: *Metall. Mater. Trans. A*, 2016, vol. 47A, pp. 2517–28.
35. C.-H. Kuo, N. Sridharan, T. Han, M.J. Dapino, and S.S. Babu: *Sci. Technol. Weld. Join*., 2019, vol. 24, pp. 382–90.
36. N. Sridharan, P. Wolcott, M. Dapino, and S.S. Babu: *Sci. Technol. Weld. Join*., 2016, vol. 22, pp. 373–80.
37. N. Sridharan, J. Poplawsky, A. Vivek, A. Bhattacharya, W. Guo, H. Meyer, Y. Mao, T. Lee, and G. Daehn: *Mater. Charact*., 2019, vol. 151, pp. 119–28.
38. N. Sridharan, D. Isheim, D.N. Seidman, and S.S. Babu: *Scripta Mater*., 2017, vol. 130, pp. 196–99.
39. I.J. Beyerlein, J.R. Mayeur, S. Zheng, N.A. Mara, J. Wang, and A. Misra: *Proc. Natl Acad. Sci. U S A*, 2014, vol. 111, pp. 4386–90.
40. A. Misra and L. Thilly: *MRS Bull*., 2012, vol. 37, pp. 965–72.
41. A.A. Ward and Z.C. Cordero: *Scripta Mater*., 2020, vol. 177, pp. 101–05.
42. J.M. Sietins, J.W. Gillespie, and S.G. Advani: *J. Mater. Res*., 2014, vol. 29, pp. 1970–77.
43. P.J. Wolcott, N. Sridharan, S.S. Babu, A. Miriyev, N. Frage, and M.J. Dapino: *Sci. Technol. Weld. Join*., 2016, vol. 21, pp. 114–23.
44. J.O. Obielodan, B.E. Stucker, E. Martinez, J.L. Martinez, D.H. Hernandez, D.A. Ramirez, and L.E. Murr: *J. Mater. Process. Technol*., 2011, vol. 211, pp. 988–95.
45. R. Hahnlen and M.J. Dapino: *Composites B*, 2014, vol. 59, pp. 101–08.
46. A. Rohatgi: WebPlotDigitizer, https://automeris.io/WebPlotDigitizer. Accessed 1 Nov 2020.
47. J. Dixon: *Meas. Control*, 1987, vol. 20, pp. 11–16.
48. V. Button: *Principles of Measurement and Transduction of Biomedical Variables*, Academic, Amsterdam, 2015, pp. 101–54.
49. A.S. Morris and R. Langari: *Measurement and Instrumentation: Theory and Application-Chapter*, Auris Reference Limited, London, 2012.
50. Omega: *Thermocouple Sensors, Connected Wire, Surface Probes Accessories*. Omega, Norwalk.
51. Omega: *Unsheathed Fine Gage Thermocouples*. Omega, Norwalk.
52. Newportus: *Unsheathed Fine Gage Thermocouples—J, K, T, E, R and S*, Newport Electronics, Santa Ana, 2020.
53. Lake Shore Cryotronics: *Cernox Technical Specifications*, Lake Shore Cryotronics, Westerville, 2019.
54. W.F. Gale and T.C. Totemeier: *Smithells Metals Reference Book*, Elsevier, Amsterdam, 2004.
55. N. Matsuno and H. Oikawa: *Can. Metall. Q*., 1975, vol. 14, pp. 315–18.
56. P. Shewmon: *Diffusion in Solids, The Minerals, Metals and Materials Series*, 2nd ed., Springer, Cham, 1979.
57. R.W. Balluffi, S.M. Allen, and W.C. Carter: *Kinetics of Materials*, Wiley, Hoboken, 2005.
58. J. Philibert: *J. Basic Princ. Diffus. Theory Exp. Appl*., 2005, vol. 2, pp. 1–10.
59. A. Einstein: *Investigations on the Theory of Brownian Movement*, Dover Publications, Inc., New York, 1956.
60. A. Smigelskas and E. Kirkendall: *AIME*, 1946, vol. XIII, p. 130.
61. H. Nakajirna: *JOM*, 1997, vol. 49, pp. 15–19.
62. K.L. Murty and I. Charit: *An Introduction to Nuclear Materials*, Wiley, Weinheim, 2013.
63. H. Mehrer: *Diffusion in Solids*, Springer, Berlin, 2007.
64. J.R. Manning and L.J. Bruner: *Am. J. Phys*., 1968, vol. 36, pp. 922–23.
65. J.R. Manning: *Acta Mater*., 1967, vol. 15, pp. 817–26.
66. P.C.W. Holdsworth and R.J. Elliot: *Philos. Mag. A*, 1985, vol. 54, pp. 601–18.
67. P.C. Holdsworth and R.J. Elliot: *Philos. Mag. A*, 1986, vol. 54, pp. 601–18.
68. I.V. Belova and G.E. Murch: *Philos. Mag. A*, 1999, vol. 80, pp. 1469–79.
69. K. Compaan and Y. Haven: *Trans. Faraday Soc*., 1956, vol. 52, pp. 786–801.
70. G.L. Montet: *Phys. Rev B*, 1973, vol. 7, pp. 650–62.
71. W.G. Wolfer: *Fundamental Properties of Defects in Metals*, Elsevier, Inc., Amsterdam, 2012, vol. 1.
72. M. Fujimoto: *Thermodynamics of Crystalline States*, Springer, New York, 2010, vol. 53.
73. W.P. Davey: *Phys. Rev*., 1925, vol. 25, pp. 753–61.
74. R. Reed-Hill: *Physical Metallurgy Principles*, 4th ed., D Van Nostrand Company, Princeton, 1964.
75. R. Smallman and A. Ngan: *Modern Physical Metallurgy*, Buttersworth & Co., 2013, pp. 287–316.
76. G.E. Dieter: *Mechanical Metallurgy*, 3rd ed., McGraw-Hill, New York, 2016.
77. W.L. Johnson: *Prog. Mater. Sci*., 1986, vol. 30, pp. 81–134.
78. RW Chan: *Nature*, 1978, vol. 273, p. 491.
79. F. Gorecki: *Scripta Mater*., 1977, vol. 11, p. 1051.
80. R.E. Stoller: *Compr. Nucl. Mater*., 2012, vol. 1, pp. 293–332.
81. R.S. Averback: *J. Nucl. Mater*., 1994, vol. 216, pp. 49–62.
82. K. Nordlund, S.J. Zinkle, A.E. Sand, F. Granberg, R.S. Averback, R.E. Stoller, T. Suzudo, L. Malerba, F. Banhart, W.J. Weber, F. Willaime, S.L. Dudarev, and D. Simeone: *J. Nucl. Mater*., 2018, vol. 512, pp. 450–79.
83. S.J. Zinkle: *Compr. Nucl. Mater*., 2012, vol. 1, pp. 65–98.
84. H. Okamoto and T.B. Massalski: *Phase Diagrams for Binary Alloys*, ASM International, 1991, pp. 16–30.
85. J. Wang, X. Lu, B. Sundman, and X. Su: *CALPHAD*, 2005, vol. 29, pp. 263–68.
86. S. Elangovan, S. Semeer, and K. Prakasan: *J. Mater. Process. Technol*., 2009, vol. 209, pp. 1143–50.
87. C. Zhang and L. Li: *Metall. Mater. Trans. B*, 2009, vol. 40B, pp. 196–207.
88. Z. Feng, S.S. Babu, B.W. Riemer, M.L. Santella, J.E. Gould, and M. Kimchi: *Weld. Res. Abroad*, 2003, vol. 49, pp. 29–35.
89. R.J. Borg and G.J. Dienes: *An Introduction to Solid State Diffusion*, Academic, Boston, 1988.
90. C.J. Simensen: *Metall. Mater. Trans. A*, 1989, vol. 20A, p. 191.
91. C. Qiu and R. Metselaar: *J. Alloy Compd*., 1994, vol. 216, pp. 55–60.
92. L.M. Foster, G. Long, and M.S. Hunter: *J. Am. Ceram. Soc*., 1956, vol. 39, pp. 1–11.
93. K.S. Hari Kumar and V. Raghavan: *J. Phase Equilib*., 1991, vol. 12, pp. 275–86.
94. Q. Mao: *Understanding the Bonding Process of Ultrasonic Additive Manufacturing*, University of Clemson, 2016.
95. D. Pal and B. Stucker: *J. Appl. Phys*. https://doi.org/10.1063/1.4807831.
96. M.R. Sriraman, H.T. Fujii, M. Gonser, S.S. Babu, and M. Short: *21st Annu. Int. Solid Free Fabr. Symp. Addit. Manuf. Conf. SFF 2010*, 2010, pp. 372–82.
97. H. Ji, J. Wang, and M. Li: *2012 Int. Conf. Electron. Packag. Technol. High Density Packag*., 2012, pp. 1586–89.
98. N. Sridharan, M.N. Gussev, C.M. Parish, D. Isheim, D.N. Seidman, K.A. Terrani, and S.S. Babu: *Mater. Charact*., 2018, vol. 139, pp. 249–58.
99. H.T. Fujii, M.R. Sriraman, and S.S. Babu: *Metall. Mater. Trans. A*, 2011, vol. 42A, pp. 4045–55.

100. R.W. Cahn: *Recovery and Recrystallization*, 4th ed., Elsevier B.V., Amsterdam, 1996.
101. K. Huang and R.E. Logé: *Mater. Des.*, 2016, vol. 111, pp. 548–74.
102. K. Aust and J. Rutter: *Trans. AIME*, 1959, vol. 215, p. 119.
103. Q. Ma, C.L. Liu, J.B. Adams, and R.W. Balluffi: *Acta Metall. Mater.*, 1993, vol. 41, pp. 143–51.
104. Y. Mishin and C. Herzig: *Mater. Sci. Eng. A*, 1999, vol. A260, pp. 55–71.
105. Y. Mishin, C. Herzig, J. Bernardini, and W. Gust: *Int. Mater. Rev.*, 1997, vol. 42, pp. 155–78.
106. J.I. Goldstein, D.E. Newburg, P. Echlin, D.C. Joy, C. Fiori, and E. Lifshin: *Scanning Electron Microscopy and Microanalysis*, Plenum Press, New York, 1975.
107. J.E. Mueller, J.W. Gillespie, and S.G. Advani: *Scanning*, 2013, vol. 35, pp. 327–35.
108. R.Z. Valiev, R.K. Islamgaliev, and I.V. Alexandrov: *Prog. Mater. Sci.*, 2000, vol. 45, pp. 103–89.
109. M.C. Chen, C.C. Hsieh, and W. Wu: *Met. Mater. Int.*, 2007, vol. 13, pp. 201–05.
110. M.C. Chen, H.C. Hsieh, and W. Wu: *J. Alloys Compd.*, 2006, vol. 416, pp. 169–72.
111. S. Ohsaki, S. Kato, N. Tsuji, T. Ohkubo, and K. Hono: *Acta Mater.*, 2007, vol. 55, pp. 2885–95.
112. D. Raabe, S. Ohsaki, and K. Hono: *Acta Mater.*, 2009, vol. 57, pp. 5254–63.
113. R. Jamaati and M.R. Toroghinejad: *Mater. Sci. Technol.*, 2011, vol. 27, pp. 1101–08.
114. Y. Saito, H. Utsunomiya, N. Tsuji, and T. Sakai: *Acta Mater.*, 1999, vol. 47, p. 579.
115. N. Tsuji, Y. Saito, S.H. Lee, and Y. Minamino: *Adv. Eng. Mater.*, 2003, vol. 5, pp. 338–44.
116. N. Tsuji, Y. Saito, H. Utsunomiya, and S. Tanigawa: *Scripta Mater.*, 1999, vol. 40, pp. 795–800.
117. R. Jamaati and M.R. Toroghinejad: *Mater. Sci. Eng. A*, 2010, vol. 527, pp. 2320–26.
118. B. Langenecker: *IEEE Trans. Sonics Ultrason.*, 1966, vol. 13, pp. 1–8.
119. D. Hull and D.J. Bacon: *Introduction to Dislocations*, 5th ed., Elsevier Ltd., Oxford, 2011.
120. D.S. Colanto: *Electrical Resistivity Measurements to Assess Vacancy Concentration in Aluminum During Ultrasonic Deformation and Vibratory Consolidation of Aluminum-Carbon Nanotube Composites*, Northeastern University, 2010.
121. V.E. Cosslett and R.N. Thomas: *Br. J. Appl. Phys*, 1964, vol. 15, pp. 1283–1300.
122. D.B. Williams and C.B. Carter: *Transmission Electron Microscopy*, Springer, New York, 2011.

Publisher's Note Springer Nature remains neutral with regard to jurisdictional claims in published maps and institutional affiliations.